STRUCTURAL BIOLOGY

Structure and assembly of CAV1 8*S* complexes revealed by single particle electron microscopy

Bing Han[1,2]*, Jason C. Porta[3]*, Jessica L. Hanks[3], Yelena Peskova[1,2], Elad Binshtein[4†], Kelly Dryden[2], Derek P. Claxton[5], Hassane S. Mchaourab[5], Erkan Karakas[5], Melanie D. Ohi[3,6‡], Anne K. Kenworthy[1,2‡]

Copyright © 2020 The Authors, some rights reserved; exclusive licensee American Association for the Advancement of Science. No claim to original U.S. Government Works. Distributed under a Creative Commons Attribution NonCommercial License 4.0 (CC BY-NC).

Highly stable oligomeric complexes of the monotopic membrane protein caveolin serve as fundamental building blocks of caveolae. Current evidence suggests these complexes are disc shaped, but the details of their structural organization and how they assemble are poorly understood. Here, we address these questions using single particle electron microscopy of negatively stained recombinant 8*S* complexes of human caveolin 1. We show that 8*S* complexes are toroidal structures ~15 nm in diameter that consist of an outer ring, an inner ring, and central protruding stalk. Moreover, we map the position of the N and C termini and determine their role in complex assembly, and visualize the 8*S* complexes in heterologous caveolae. Our findings provide critical insights into the structural features of 8*S* complexes and allow us to propose a model for how these highly stable membrane-embedded complexes are generated.

INTRODUCTION

As early as the 1950s, the presence of flask-shaped plasma membrane invaginations was noted in endothelial cells (*1*). It is now recognized that the surfaces of a wide range of cell types are decorated by these 50 to 100 nm structures known as caveolae (*2*). Caveolae have several unique features that distinguish them from other types of coated vesicles. The membranes in caveolae are not continuously curved, but rather exhibit a polygonal-like appearance (*3*, *4*). They are relatively uniform in size and assemble in an all-or-none fashion (*2*, *5*). Although they can undergo endocytosis, they spend most of their life cycle attached to the plasma membrane in the form of open flasks (*2*). They can also undergo reversible flattening to serve as membrane reservoirs (*2*, *4*, *6*).

The 21-kDa integral membrane protein caveolin 1 (CAV1) is an essential structural component of caveolae and the founding member of the caveolin gene family (*2*). Caveolin family members share a similar membrane topology and contain multiple domains. For the case of CAV1, this includes an N-terminal region (residues 1 to 101), a hairpin-like intramembrane domain (residues 102 to 134), and a C-terminal domain (residues 135 to 178) (fig. S1). Contained within the N-terminal region are a predicted unstructured region and several partially overlapping domains including a highly conserved signature motif (residues 68 to 75), an oligomerization domain (residues 61 to 101), and a scaffolding domain (residues 82 to 101). The C-terminal domain is thought to fold into a long α helix and contains three palmitoylation sites (*7*, *8*). It has also been predicted to potentially contain a β strand in the extreme C-terminal region (*9*). The 33-residue intramembrane domain forms an unusual reentrant helix-break-helix structure (*10*), defining caveolin as a member of the poorly understood class of monotopic membrane proteins (*11*). This hairpin-like domain inserts into the cytoplasmic face of the plasma membrane, placing both the N and C terminus in the cytoplasm.

Shortly after CAV1 was first identified as a key component of caveolae, the protein was shown to self-assemble into highly stable high–molecular weight oligomers (*12*, *13*). These oligomers assemble cooperatively shortly after CAV1 is synthesized (*13*), are estimated to contain 7 to 14 copies of CAV1 (*12*–*14*), and are ~8*S* in size when analyzed by velocity gradient centrifugation (*15*). The formation of these oligomers is an essential step in caveolae biogenesis, as mutant versions of the protein that fail to generate oligomers are incapable of supporting caveolae assembly (*16*). When they traffic through the Golgi complex, 8*S* complexes further oligomerize in a cholesterol-dependent manner into higher-order 70*S* complexes (*15*). The 70*S* complexes later become incorporated into the plasma membrane where they recruit caveolae accessory proteins such as the cavins that assist in sculpting caveolar membranes, as well as other proteins that regulate caveolae dynamics to ultimately generate mature caveolae (*15*, *17*).

Some effort has been made to characterize the structural features of CAV1 monomers, but a three-dimensional (3D) structure of the protein is still lacking (*7*, *8*). Furthermore, little is known about the structure of 8*S* oligomers or how caveolin monomers are packaged within them. Early studies suggested that CAV1 oligomers are organized either into 4 to 6 nm spherical particles (*12*) or filaments composed of rings (*14*). However, more recent studies point to a disc-like organization of the structures. The 8*S* complexes purified from mammalian cells are disc-shaped structures 15 to 17 nm in diameter with a thickness of 5 nm (*3*). The most detailed structural insights into the 8*S* complexes come from electron microscopy (EM) analysis of complexes formed by the muscle-specific caveolin family member, CAV3. CAV3 is ~65% identical and ~85% similar to CAV1, and like CAV1, CAV3 assembles into high–molecular weight oligomers and drives caveolae formation (*18*). Single particle EM analysis of negatively stained CAV3 complexes at a resolution of ~17 Å revealed that

[1]Center for Membrane and Cell Physiology, University of Virginia, Charlottesville, VA, USA. [2]Department of Molecular Physiology and Biological Physics, University of Virginia School of Medicine, Charlottesville, VA, USA. [3]Life Sciences Institute, University of Michigan, Ann Arbor, MI, USA. [4]Center for Structural Biology, Vanderbilt University, Nashville, TN, USA. [5]Department of Molecular Physiology and Biophysics, Vanderbilt University School of Medicine, Nashville, TN, USA. [6]Department of Cell and Developmental Biology, University of Michigan School of Medicine, Ann Arbor, MI, USA.
*These authors contributed equally to this work.
†Present address: Vanderbilt Vaccine Center, Vanderbilt University Medical Center, Nashville, TN, USA.
‡Corresponding author. Email: mohi@umich.edu (M.D.O.); akk7hp@virginia.edu (A.K.K.)

the protein assembles into toroidal structures with a diameter of ~165 Å and a height of ~55 Å that consist of nine copies of CAV3 organized into a wedge-like structure (*19*). On the basis of gold labeling studies, the C-terminal domains of the monomers have been proposed to be positioned within the center of the complex (*19*).

Together with structural data for the cavins, recent EM structures of CAV1 and CAV3 complexes have led to the current model of caveolae organization (*3*, *4*). According to this model, 8*S* complexes form flat faces of the polyhedral-like membranes of caveolae and are surrounded by a network of filaments generated by cavins, which enforce the polyhedral architecture of caveolar membranes (*3*, *4*). Yet, key questions about the structure of caveolae and its fundamental building blocks remain unanswered, including how caveolin monomers are packaged within 8*S* complexes, how the complexes are assembled, whether the overall structural elements of 8*S* complexes are conserved between caveolin family members, and how they interact with one another and accessory proteins to bend membranes and generate caveolae.

CAV1 is not only capable of inducing caveolae biogenesis in eukaryotes; the expression of mammalian CAV1 also drives the formation of caveolae-like structures in *Escherichia coli* (*9*, *20*). Termed heterologous caveolae (*h*-caveolae), these caveolin-induced vesicles bud from the inner membrane into the bacterial cytoplasm where they accumulate in the form of closed vesicles. Despite their bacterial origins, *h*-caveolae recapitulate several key properties of mammalian caveolae: They are similar in size, are thought to contain similar numbers of CAV1 molecules, and are composed of high–molecular weight CAV1 oligomers (*20*). Furthermore, *h*-caveolae exclude detectable levels of bacterial proteins (*20*). These findings suggest *E. coli h*-caveolae represent a useful model to investigate the structure of CAV1 in a system where it both oligomerizes and induces membrane curvature. Here, we used *E. coli* as a model system to study the organization of CAV1 8*S* complexes, mapped the positions of key regions of the protein, determined which domains contribute to complex assembly, and visualized the 8*S* complexes within *h*-caveolae.

RESULTS

CAV1 forms 8*S*-like complexes in *E. coli*

Previous work has shown that CAV1 forms high–molecular weight complexes when expressed in *E. coli* (*20*), but the molecular organization of these complexes was not determined. To address this question, we first screened for conditions that would retain oligomeric assembly of CAV1 after they were extracted from the membrane. We initially performed fluorescence-coupled size exclusion chromatography (FSEC) analysis of CAV1-Venus fusion proteins extracted using different detergents (*21*). Upon further analysis of CAV1 purified using select detergents, we concluded that *n*-dodecyl-β-maltopyranoside (C12M) is the best detergent for purification of CAV1 8*S* complexes. Total membrane proteins were extracted using 2% C12M from *E. coli* cells expressing wild-type (WT) human CAV1α with a C-terminal 6X-Histidine tag (WT CAV1). Detergent-solubilized WT CAV1 oligomers were separated from the protein lysate by Ni-sepharose affinity followed by gel filtration chromatography. Two major peaks were observed in the elution profile: a broad peak containing two subpeaks (peaks 1a and 1b) and a second sharper peak (peak 2) (Fig. 1A). SDS–polyacrylamide gel electrophoresis (SDS-PAGE) and Coomassie staining of individual fractions indicate each peak contains a ~22-kDa protein, which is consistent with the molecular weight of CAV1 (Fig. 1B). The presence of CAV1 was confirmed by Western blotting of the SDS-PAGE gels (Fig. 1C).

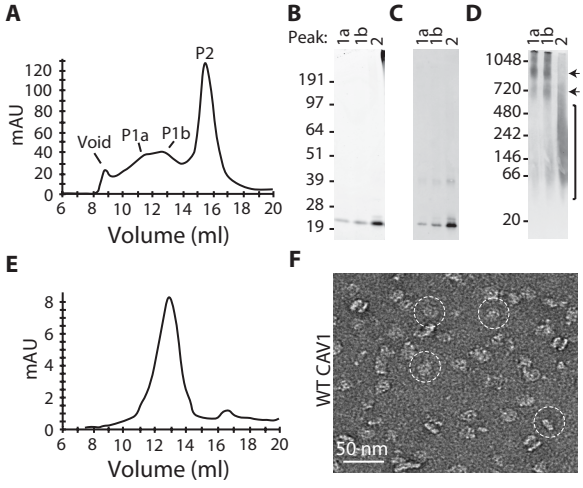

Fig. 1. Purification of 8*S* WT CAV1 complexes from *E. coli*. (**A**) Gel filtration profile of detergent solubilized WT CAV1 oligomers. The position of the void and peaks P1a, P1b, and P2 are labeled. mAU, milli-absorbance unit. (**B**) Coomassie-stained SDS-PAGE gel and (**C**) Western blot analysis show that each peak is composed of CAV1. (**D**) Native gel of P1a, P1b, and P2 shows CAV1 is present in high–molecular weight oligomeric complexes. Arrows show location of high–molecular weight oligomers typical of 8*S*-like complexes. Bracket shows location of lower–molecular weight oligomeric complexes. (**E**) Gel filtration profile of WT CAV1 oligomers from P1b run a second time over the gel filtration column. One major peak was observed. (**F**) Representative negative stain image of particles from the WT CAV1 peak isolated in (E). A few examples of the 8*S* particles are circled. Scale bar, 50 nm.

A characteristic feature of 8*S* complexes is their migration as high–molecular weight complexes on blue native gels (*16*, *22*). To assess the size of the complexes, we performed blue native electrophoresis-based Western blot analysis. CAV1 in peaks 1a and 1b migrated in multiple high–molecular weight complexes with molecular masses around or greater than 720 kDa in size (Fig. 1D), similar to the molecular mass of CAV1 8*S* complexes extracted from mammalian cells (*22*). CAV1 found in the second peak migrated in lower molecular mass complexes ranging between 40 and 500 kDa (Fig. 1D). These findings suggest that CAV1 derived from *E. coli* membranes can generate 8*S*-like complexes and smaller oligomers.

Fractions from the peaks were further examined using negative stain electron microscopy. All contained disc-shaped particles (fig. S2). However, the particles in peaks 1a and 1b were larger and appeared more homogenous than the smaller, more heterogenous complexes isolated in peak 2 (fig. S2). Further inspection revealed that particles in peaks 1a and 1b are disc shaped. Both "en face" and side views of the complexes were apparent, including both individual complexes and dimerized discs (fig. S2, A, B, and D). To improve homogeneity of the discs, fractions encompassing peak 1b were run a second time over gel filtration. One peak was recovered and visualized using negative stain EM (Fig. 1, E to F). This fraction was used for further analysis of the 8*S* WT CAV1 complexes.

CAV1 assembles into disc-shaped complexes that contain a central stalk

To better characterize the structural features of the 8*S* WT CAV1 complexes, we collected a dataset of ~16,000 negatively stained particles

of CAV1. The particles were classified into 20 two-dimensional (2D) class averages using RELION (fig. S3A) (*23*). This analysis revealed classes corresponding to both the en face and side views of 8*S* CAV1 complex (Fig. 2A). The en face view consists of disc-shaped complexes that are ~15 nm in diameter (fig. S4A and table S1). The disc structure is composed of two rings: an ~4.2-nm wide outer ring and an ~2-nm-wide inner ring (Fig. 2, A and B). The side view reveals a T-shaped structure consisting of a thin, flat cap that is ~15 nm wide and ~4.8 nm thick and a central small protruding stalk that is ~3.6 nm wide (Fig. 2, A and B). The stalk emanates from the inner ring seen in the en face view. Some side view classes showed dimerized 8*S* CAV1 discs that appeared to be interacting through the stalk region (Fig. 2A, bottom right, and fig. S3A).

The outer ring in the en face view of the 2D averages appeared to be composed of distinct globular domains (Fig. 2A), although there was variability between classes on how well-defined and how many of these regions were clearly visible. To quantify the size and number of these domains, we measured the intensity of the stain distribution along the edge of one of the en face 2D averages where the densities in the outer ring were well defined (Fig. 2C and fig. S4B). This analysis revealed that there are ~10 repeating globular domains in this class average that are each ~4.4 nm wide (Fig. 2C and fig. S4, B and C). We hypothesize these repeating densities may represent CAV1 monomers within the 8*S* complex, although the variability of the stain distribution in the other classes makes it difficult to repeat this type of analysis in the less well-defined class averages.

The C-terminal region of CAV1 localizes to the stalk region and the N terminus is localized to the periphery of the discs

There is evidence suggesting that the C terminus of CAV3 is localized to the center of 8*S* complexes (*19*). However, data supporting this model were principally based on limited labeling by C-terminally directed antibodies (*19*). We therefore sought to directly probe the position of the N and C termini of CAV1 within the 8*S* complexes. For these studies, we generated fusions of CAV1 with large tags to serve as fiduciary markers enabling us to trace out the orientation of CAV1 within the complex. We found that addition of C-terminal Venus tag or an N-terminal MBP (maltose-binding protein) tag was permissive for 8*S* complex formation (fig. S5, A and B) and used these constructs for further studies.

We first examined the C-terminally labeled CAV1-Venus construct. En face views of both individual CAV1-Venus 8*S* complexes and class averages appeared to be similar to the CAV1 8*S* complexes in shape (Fig. 2, A, B, D, and E) but had a slightly larger diameter (fig. S4A). An extra density extending from the stalk region was clearly visible in side views of CAV1-Venus complexes (Fig. 2, D and E). This "fan-shaped" structure emanating from the stalk region of the CAV1-Venus complexes was absent in side views of CAV1 8*S* complexes (Fig. 2A). These findings suggest that the C terminus of CAV1 is localized to the central stalk region of the 8*S* complex. Because the C terminus of CAV1 is known to face the cytoplasm, this additionally suggests that the flat face of the cap is the side of the complex that faces the membrane.

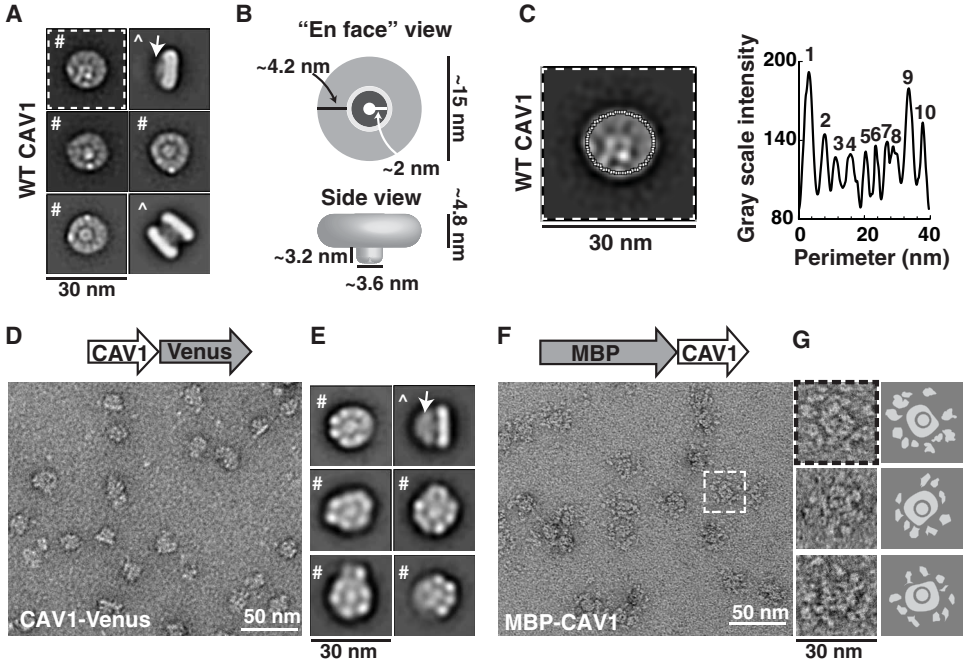

Fig. 2. Organization of 8*S* WT CAV1 complexes. (**A**) Representative 2D class averages of 8*S* CAV1 oligomers. #, en face view; ^, side view; arrow, protruding stalk. 2D average with outlined by dashed line also shown in (C). Scale bar, 30 nm. (**B**) Cartoon model depicting features and measurements seen in class averages. (**C**) The gray scale intensity around the perimeter of a 2D class average of WT CAV1 as determined using ImageJ. The positions of the oval used for analysis is shown in white dotted lines on the class average image. The graph shows the gray scale intensity around the complex perimeter. Numbers indicate the position of individual peaks within the profile, presumed to correspond to CAV1 monomers. (**D**) Representative image of negatively stained CAV1-Venus 8*S* complexes. A schematic of the CAV1-Venus construct is shown above image. Scale bar, 50 nm. (**E**) Representative 2D averages of CAV1-Venus 8*S* complexes. #, en face view; ^, side view; arrow, protruding stalk and Venus tag. Scale bar, 30 nm. (**F**) Representative image of negatively stained MBP-CAV1 8*S* complexes. A schematic of the MBP-CAV1 construct is shown above image. The dashed white box highlights one 8*S* MBP-CAV1 disc. Scale bar, 50 nm. (**G**) Examples of individual MBP-CAV1 discs (left) and corresponding cartoon schematics of each particle (right) showing the central disc surrounded by MBP petals. Particle with dashed box is the same complex highlighted in (F). Scale bar, 30 nm.

We next evaluated the orientation of the N terminus of CAV1 using the MBP-CAV1 construct. MBP-CAV1 complexes displayed a sunflower-like pattern, with a central disc structure surrounded by flexible "petals" (Fig. 2, F and G). The variability of the positions of the MBP densities made it impossible to generate interpretable 2D class averages. Nevertheless, inspection of images of individual MBP-CAV1 8*S* complexes clearly shows that the N terminus (i.e., the MBP) is arrayed around the outer ring of the 8*S* disc. The distance and position of the MBP densities relative to the disc varied, suggesting that the N terminus is flexible (Fig. 2, F and G).

The C terminus of CAV1 is essential for maintaining the disc shape of the 8*S* complex

A notable structural feature of the CAV1 8*S* complex is the protruding C-terminal stalk (Fig. 2, A and B). To better understand which regions of the C terminus contribute to stalk assembly, we generated a series of the C-terminal truncations of CAV1 (Fig. 3A). They included constructs designed to disrupt the predicted β strand located in the extreme C terminus (*9*). These constructs were expressed in *E. coli*, and the resulting complexes were subsequently purified (fig. S5, C and D) and examined by negative stain EM (Fig. 3, B and C, and fig. S6, A and B).

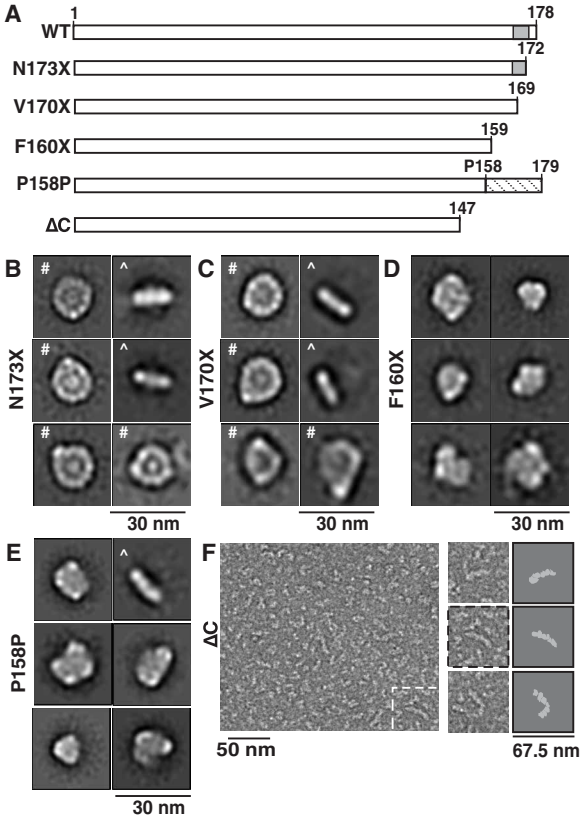

Fig. 3. The C terminus of CAV1 is required for stalk formation and maintaining the disc shape of the 8*S* complexes. (**A**) Schematic of CAV1 constructs used to test the importance of the C terminus of CAV1. Gray box, predicted position of β strand. Dashed box, new C-terminal residues introduced by the P158P frameshift. (**B** to **E**) Representative class averages of N173X (B), V170X (C), F160X (D), and P158P (E). #, en face view; ^, side view. Scale bars, 30 nm. (**F**) Representative negative stain image of CAV1 ΔC (left). The dashed white box highlights one linear oligomer. Scale bar, 50 nm. Examples of individual linear ΔC oligomers (middle) and cartoon schematic of each particle (right) are also shown. Particle with dashed box is the same oligomer highlighted in left panel. Scale bar, 67.5 nm.

The two shortest truncations, N173X and V170X (Fig. 3A), formed disc-shaped complexes. En face views showed that the complexes were generally similar in size and shape as WT CAV1 8*S* complexes (Fig. 3, B and C, and fig. S3, C and D). However, N173X contained a smaller protrusion, and the side views of N170X completely lacked a protruding stalk (Fig. 3, B and C). Furthermore, a fraction of the V170X complexes had a less defined inner ring and were more heterogenous and less circular than WT CAV1 or N173X complexes (Fig. 3C and fig. S3D). These results suggest that the extreme C-terminal amino acids are required for the generation of the stalk and contribute to the organization of the inner ring region and overall disc shape of the complex.

To further probe the role of the CAV1 C terminus in 8*S* complex organization, we examined a naturally occurring disease-associated mutation of CAV1, F160X. Identified in a patient with congenital generalized lipodystrophy (CGL) and pulmonary arterial hypertension (PAH), F160X lacks the last C-terminal 19 amino acids of CAV1 (Fig. 3A) (*24*–*26*). Negative stain analysis showed that F160X complexes varied in both size and shape and failed to adopt a uniform disc-like organization or display a clear central stalk (Fig. 3D and figs. S3E and S6C). Thus, at least a subset of residues 160 to 178 is required for the creation of the stalk and the regularity of the discs.

For comparison, we also examined the structural organization of P158P, another naturally occurring PAH disease mutant (*27*, *28*). Unlike F160X, which results in a truncation, the frameshift mutation in P158P gives rise to a novel CAV1 C terminus that is one residue longer than that of WT CAV1 (Fig. 3A) (*27*, *28*). Although the C termini of P158P and WT CAV1 contain essentially the same number of amino acids (Fig. 3A), CAV1-P158P complexes were structurally heterogenous and more similar in appearance to F160X complexes than to WT CAV1 complexes (Figs. 2A and 3, D and E, and fig. S6, C and D). Furthermore, a 2D average of a side view of the P158P complex revealed that the central stalk is missing (Fig. 3E, right top, and fig. S3F). This indicates the specific amino acid sequence of residues 159 to 178 is required to assemble the stalk structure and to maintain the correct size and shape of the discs.

We next examined the importance of residues 148 to 178 in forming CAV1 complexes using a ΔC construct (Fig. 3A). The ΔC truncation is predicted to eliminate a portion of a long C-terminal α helix of CAV1 (residues 132 to 175) (*29*) and a portion of a secondary site identified as important for oligomerization (residues 134 to 154) (*30*). Negative stain analysis of this construct revealed no disc-like structures; instead, we observed heterogenous structures, including some examples of chains of globular domains adopting a "snake-like" appearance (Fig. 3F). This suggests that residues 1 to 147 are sufficient to support the assembly of linear oligomers. In addition, because closed discs were seen for F160X but not for ΔC, residues 148 to 159 appear to contribute to disc closure.

The N terminus of CAV1 is also required to generate disc-shaped 8*S* complexes

We next examined the contributions of the N terminus to the assembly and structural integrity of 8*S* complexes. We first studied the naturally occurring β-isoform of CAV1, CAV1β (Fig. 4A). CAV1β lacks the first 31 amino acids of the protein but can assemble into caveolae and is the predominant CAV1 isoform in certain types of mammalian cells (*31*). We examined two CAV1β constructs, one

tagged with a 6X His-tag at the C terminus and another containing a C-terminal Venus tag. When expressed in *E. coli*, both versions of CAV1β generated 8*S*-like complexes (figs. S3, G and H; S5, H and I; and S6, E and F). The purified CAV1β complexes form discs that contain well-defined inner and outer rings but are slightly smaller in diameter than observed for full-length CAV1 (~13.5 nm versus ~15 nm) (Fig. 4, B and C; fig. S4A; and table S1). The CAV1β-Venus oligomers were more homogeneous than the CAV1β complexes as seen in negative stain 2D averages (Fig. 4, B and C, and fig. S3, G and H), suggesting that the addition of Venus to the C terminus may help stabilize the complex. 2D averages of the side view of the complex of CAV1β revealed the presence of a central stalk-like protrusion similar to that seen in WT CAV1 complexes, as well as additional fan-shaped density emerging from the stalk for the CAV1β -Venus complexes (Fig. 4, B and C). Thus, the first N-terminal 31 amino acids of CAV1α, which are missing in CAV1β, are not required for the assembly of the disc-like 8*S* complex or the central protrusion.

Residues 1 to 48 of CAV1 are predicted to reside within a structurally disordered region of the protein (*7*) and are dispensable for caveolae biogenesis to occur in mammalian cells (*5*). To understand how they contribute to the structure of the 8*S* complex, we next examined a construct lacking the first 48 amino acids of the N-terminal domain, ΔN. ΔN failed to assemble into discs. Instead, it formed a heterogenous mixture of particles, including nonstructured protein aggregates of varying size and chains of globular domains of varying lengths with a snake-like appearance (Fig. 4D). The snake-like oligomers were generally similar in overall appearance to the structure of the ΔC oligomers (Figs. 3F and 4D, right). Thus, residues 49 to 178 can support the assembly of linear and irregular structures, whereas residues 32 to 48 are additionally required to organize CAV1 oligomers into regular discs.

Given that deletion of either residues 2 to 48 or 148 to 178 of CAV1 gave rise to linear oligomers in our 8*S* complex assembly assay, we wondered whether residues 49 to 147 are sufficient to support oligomerization. To test this, we expressed, purified, and examined a ΔNΔC construct using negative stain. ΔNΔC retained the ability to generate high–molecular weight oligomers as assessed by fast protein liquid chromatography (fig. S5K). Negative stain analysis showed these correspond to heterogenous linear oligomers that are flexible and vary in size, in addition to smaller oligomeric structures (Fig. 4E). We conclude that residues 49 to 147 are sufficient to support oligomerization, but not for the assembly of fully formed disc-shaped 8*S* complexes, at least when expressed in *E. coli*.

8*S* complexes are visible in *h*-caveolae

A notable consequence of expressing CAV1 in *E. coli* is the induction of *h*-caveolae (*20*). Previous studies have visualized the distribution of an MBP-tagged form of CAV1 in fixed, detergent extracted *h*-caveolae and revealed a potential polyhedral organization of ring-like MPB-CAV1 oligomers (*20*). However, because the structure of isolated CAV1 oligomers themselves was not examined, their positioning within *h*-caveolae could not be directly ascertained (*20*). We speculated that the density of Venus emanating from the C-terminal stalk in the CAV1-Venus complexes, which is predicted to face the cytoplasm, could allow us to visualize the positioning of 8*S* complexes within *h*-caveolae.

To address this question, we purified *h*-caveolae from *E. coli* expressing CAV1-Venus by affinity chromatography and imaged them by negative stain (Fig. 5A). The size of *h*-caveolae was heterogenous, with diameters ranging from 17.7 to 54.5 nm and an average diameter of 30.3 ± 8.2 nm (means ± SD, $n = 112$) (Fig. 5B). Because of this heterogeneity, we were not able to perform averaging across multiple

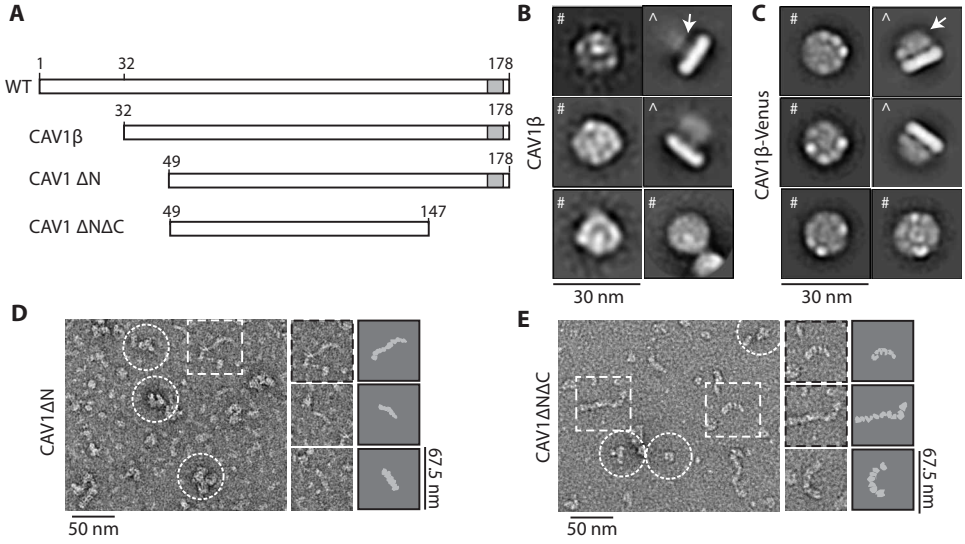

Fig. 4. Regions of the N terminus of CAV1 are required for 8*S* complex stability. (**A**) Schematic of CAV1 constructs used to test the importance of the N terminus of CAV1. Gray box, position of predicted β strand. (B and C) Representative class averages of CAV1β (**B**) and CAV1β-Venus (**C**). #, en face view; ^, side view; arrow, protruding stalk. Scale bars, 30 nm. (**D**) Representative negative stain image of CAV1 ΔN (left). Dashed white box highlights one linear ΔN oligomer and white circles highlight heterogenous aggregates. Scale bar, 50 nm. Examples of individual linear ΔN oligomers (middle) and corresponding cartoon schematic of each particle (right) are also shown. Particle with dashed box is the same oligomer highlighted in left panel. Scale bar, 67.5 nm. (**E**) Representative negative stain image of CAV1 ΔNΔC (left). Dashed white boxes highlight linear ΔNΔC oligomers and white circles highlight heterogenous aggregates. Scale bar, 50 nm. Examples of individual linear ΔN oligomers (middle) and corresponding cartoon schematic of each particle (right) are also shown. Particles with dashed box are the same oligomers highlighted in left panel. Scale bar, 67.5 nm.

h-caveolae. Nevertheless, on the edges of individual *h*-caveolae multiple examples of clustered densities similar to those observed emanating from the central stalk regions of the purified CAV1-Venus complexes could be detected by negative stain EM (Fig. 5, A and C). We repeated this experiment using WT CAV1 that lacks the Venus tag. The *h*-caveolae generated from WT CAV1 were also heterogeneous in size with diameters ranging from 15.2 to 49.7 nm and an average diameter of 30.5 ± 7.6 nm (means ± SD, $n = 102$) (Fig. 5B). They no longer had protruding densities (Fig. 5, D and E), providing additional evidence that the clustered densities represent the Venus tag emanating from the C-terminal stalk.

To determine whether the CAV1-Venus 8*S* complexes directly interact with one another, we detergent extracted the purified *h*-caveolae using 1% Triton X-100 to remove membrane lipids. This led to the loss of intact *h*-caveolae as expected. Instead, we now saw dispersed individual 8*S* complexes (Fig. 5, F to H), as well as examples of interconnected 8*S* complexes that formed arc-like arrays (Fig. 5I). 2D class averages of individual 8*S* complexes obtained from the Triton X-100 extracted sample yielded structures very similar to those obtained for purified 8*S*-like CAV1-Venus complexes (Figs. 2E and 5H). While the arrays were too flexible to generate 2D averages, they are of the proper thickness to represent CAV1-Venus 8*S* complexes (Fig. 5I). These results reinforce our findings that these disc-shaped structures correspond to functional complexes that represent the fundamental building blocks of *h*-caveolae.

DISCUSSION

Overall organization and novel structural features of the 8*S* CAV1 complex

Despite their importance in caveolae biogenesis, the structural organization of 8*S* complexes formed by the monotopic membrane protein caveolin has remained enigmatic. Here, we provide critical new insights into the architecture and assembly of recombinant human CAV1 8*S* complexes using single particle electron microscopy.

We show that detergent-solubilized, negatively stained 8*S* CAV1 complexes isolated from *E. coli* are disc shaped and exhibit a toroidal organization consisting of an outer ring of globular densities surrounding a weaker density region and a higher density central structure (Fig. 2, A and B). The overall shape of the complex is thus consistent with previous studies suggesting CAV1 has an intrinsic propensity to form disc- or ring-like structures (*3*, *14*). Many of the features of the CAV1 8*S* complex are very similar to those previously reported for negatively stained CAV3 complexes isolated from insect cells (*19*), including their overall dimensions (15 nm by 4.8 nm for CAV1 versus 16.5 nm by 5.5 nm for CAV3). A centrally located protruding

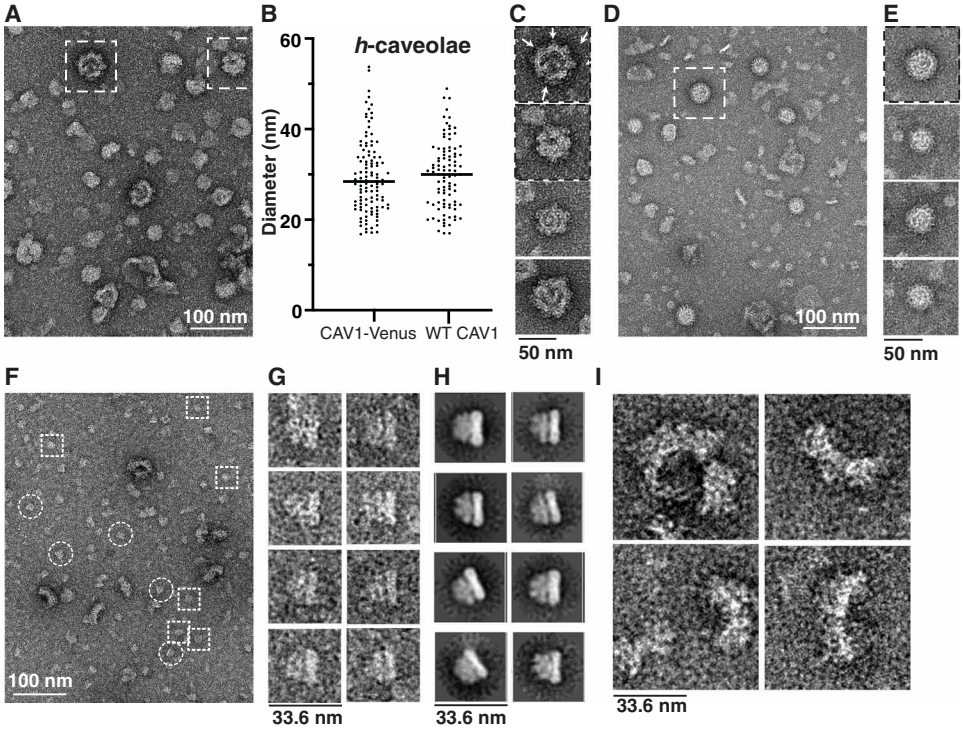

Fig. 5. Characterization of *h*-caveolae purified from *E. coli*. (**A**) Representative negative stain image of *h*-caveolae isolated from *E. coli* expressing CAV1-Venus. Scale bar, 100 nm. White dashed boxes mark *h-caveolae* shown in (C). (**B**) Diameter of 112 individual (CAV1-Venus) and 102 (WT CAV1) *h*-caveolae seen in negative stain images. (**C**) Examples of individual *h*-caveolae composed of CAV1-Venus. Arrows in top panel point to the position of visible 8*S* CAV1-Venus complexes. Scale bar, 50 nm. (**D**) Representative negative stain image of *h*-caveolae isolated from *E. coli* expressing WT CAV1. Scale bar, 100 nm. White dashed box marks *h-caveolae* shown in (E). (**E**) Examples of individual *h*-caveolae from *E. coli* expressing WT CAV1. Scale bar, 50 nm. (**F**) Representative negative stain image of isolated *h*-caveolae composed of CAV1-Venus solubilized with 1% Triton X-100. Examples of individual 8*S* CAV1-Venus particles are marked by either white circles (side views) or white squares (en face views). Scale bar, 100 nm. (**G**) Examples of individual 8*S* CAV1-Venus complexes seen in images of solubilized *h*-caveolae. All particles represent side views and have been translationally aligned. Scale bar, 33.6 nm. (**H**) Representative 2D class averages of individual 8*S* CAV1-Venus complexes obtained from images of Triton X-100 solubilized *h*-caveolae. All averages represent side views. Scale bar, 33.6 nm. (**I**) Examples of arrays of interconnected 8*S* CAV1-Venus complexes observed after solubilization with Triton X-100. Scale bar, 33.6 nm.

structure is also apparent in both complexes. For the case of CAV1, this corresponds to a stalk-like protrusion in side views (Fig. 2A), whereas for CAV3 the central structure appears to be more cone-shaped (*19*). The fact that so many similarities exist between these structures, despite having been isolated for two different caveolin family members from two different expression systems, strongly suggests that this represents the characteristic architecture of 8*S* complexes.

We hypothesize that the repeating globular units comprising the outer ring of the 8*S* complexes represent CAV1 monomers. Assuming the average diameter for WT CAV1 8*S* complexes is 14.4 nm and the average distance each monomer occupies along the circumference of the complex is 4.4 nm (fig. S4), we estimate that each WT CAV1 complex contains ~10 monomers. This value is within range of previous estimates from biochemical studies as well as the report that negatively stained CAV3 complexes contain nine monomers (*19*). Even for complexes containing WT CAV1, packing of globular domains of the protein in the outer ring of the 8*S* complexes was not regular across the entire ring; in several cases, globular domains appeared to protrude from the ring, breaking the symmetry of the structure. It is thus possible that structural heterogeneity is a native feature of the complexes.

Our results also enable us to pinpoint the position of the N and C termini within the complex. We show the N terminus of CAV1 localizes on the periphery of the outer ring and confirm it assumes a flexible conformation based on the irregular distribution of the MBP tag (Fig. 2, F and G). This is consistent with reports that the N-terminal region of CAV1 is unstructured (*7*) and the first 48 residues in particular are protease sensitive (and thus solvent accessible) in *h*-caveolae (*20*). This also strongly suggests that interactions between adjacent discs to generate higher-order oligomers, such as are expected to occur in caveolae, are mediated by the N-terminal domain of CAV1. We also provide definitive evidence that the C-terminal domain of CAV1 localizes to the center of the complex and show that it contributes to the assembly of the central stalk (Figs. 2, D and E, and 3 B and C). The resolution of the negative stain structure is too low to definitively determine the secondary structure of this region of the protein, but we speculate this could be a β barrel given the predicted propensity of the extreme C-terminal domain to form a β strand (*9*). Our findings also suggest that interactions can occur between stalks, as evidenced by the presence of dimers of WT CAV1 (Fig. 1). It remains to be determined whether this is a physiologically relevant interaction. Clearly, obtaining higher resolution structural information, such as from cryo-EM, will be essential to pinpoint the exact positioning of these and other key structural elements of CAV1 within the complex. It will also be important to examine the structure of 8*S* complexes in membrane environments, including in the presence of cholesterol, a key regulator of caveolae structure.

On the basis of the positions of the C and N terminus of CAV1 within the 8*S* complex, we can infer where other domains of the protein likely reside. The flat face of the complex, opposite of that from which the C-terminal stalk emerges, can be assigned as the membrane-associated surface of the complex given that the C terminus of CAV1 is known to face the cytoplasm. Because the N terminus is localized at the periphery of the disc, it seems likely other domains found in the N-terminal half of the protein, including the oligomerization and scaffolding domains, also reside in the outer ring. The central location of the C terminus implies that the three palmitoylation sites of CAV1 (Cys^{133}, Cys^{143}, and Cys^{156}) are likely positioned in the center of the complex. This would generate a very high density of palmitates in this area, which in turn could potentially generate a highly ordered nanodomain.

Proposed model for how 8*S* complexes assemble and how defects in assembly contribute to disease

To better understand the structural basis for the assembly of 8*S* complexes, we probed the contributions of the N- and C-terminal domains of CAV1 to their overall organization (Figs. 3 and 4). The naturally occurring CAV1β isoform, which lacks residues 1 to 31, generated disc-shaped structures similar in shape but slightly smaller than those formed by WT CAV1α (Fig. 4, B and C, and fig. S4A). In contrast, truncation of residues 2 to 48 of the N terminus more severely disrupted the size and shape of complexes, leading to the assembly of irregular aggregates and linearized chains of globular domains (Fig. 4D). Truncations of the extreme C terminus (residues 170 to 178) maintained overall disc structure but caused a loss of the central protrusion and some rearrangements within the central region of the complex (Fig. 3, B and C), whereas disease-associated mutants of the protein (F160X and P158P) generated irregular discs or aggregates (Fig. 3, D and E). Further truncation of the C terminus, either in the presence (ΔC) or absence (ΔNΔC) of an intact N terminus, ultimately led to the formation of chains of globular domains rather than toroidal discs (Figs. 3F and 4E).

Together, these findings suggest a potential mechanism for how assembly of disc-shaped 8*S* complexes occurs (Fig. 6). In this working model, CAV1 monomers can be thought of as wedge-shaped "sections" that come together to form an "orange slice" (Fig. 6A). One important set of interactions between the "wedges" occurs at the outer ring of the disc, as revealed when the C-terminal domain of CAV1 is truncated (Fig. 6B). We speculate that this oligomerization event is driven by the core region of the protein (residues 49 to 147). To support such a packing arrangement, heterotypic interactions involving at least two surfaces of each monomer would be required (Fig. 6C). While the identity of these interaction surfaces is currently unknown, the well-studied oligomerization domain likely serves as one interaction interface. Additional binding events between monomeric wedges occur within the inner ring of the complex where the C-terminal domain of CAV1 is located (Fig. 6C). This includes interactions between the extreme C-terminal domains of CAV1 to create the central tubular stalk structure, possibly via the formation of a β barrel as discussed above. We speculate that the formation of this tubular structure may not only serve as a mechanism that helps stabilize the discs but also could help define the ultimate size the discs can attain. The N-terminal domain of CAV1 also aids in the generation of regular discs. Residues 32 to 48 appear to be especially important in this process, since deletion of residues 1 to 31 support native-like complex assembly whereas deletion of residues 2 to 48 does not. While the structural basis for this activity is currently unknown, residues 30 to 50 have previously been predicted to generate an amphipathic α helix (*32*).

The "orange" model of 8*S* complex assembly has several implications. First, the organization of wedge-shaped monomers into a disc gives rise to a structure that could potentially incorporate varying numbers of n-mers. Second, this model suggests that it is unlikely that homotypic interactions between the oligomerization domains of adjacent CAV1 monomers occur, as was suggested in earlier models (*33*). Instead, it predicts that the oligomerization domain undergoes heterotypic interactions with a secondary binding site of the protein. Third, the centrally located C terminus contributes to the

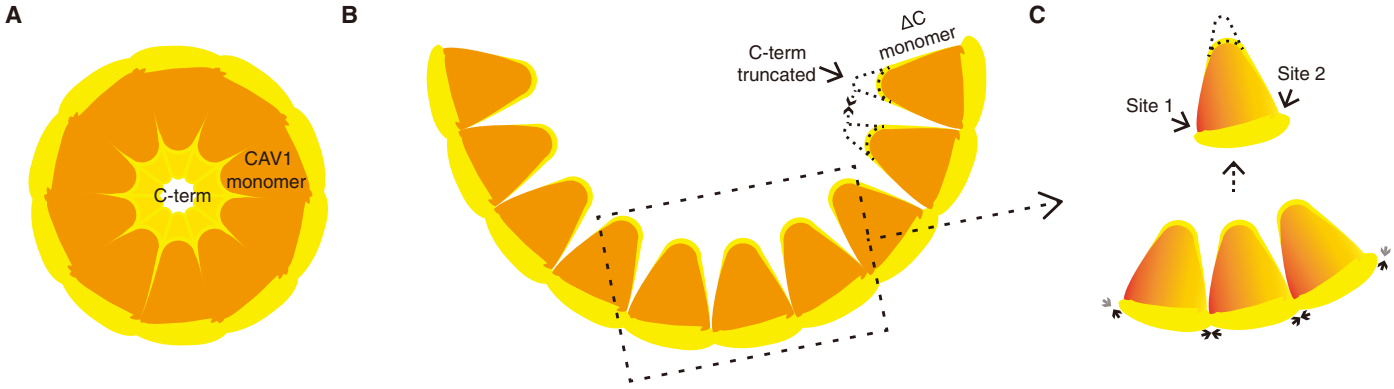

Fig. 6. "Orange" model of 8*S* complex assembly. (**A**) CAV1 monomers form wedge-like "sections" that self-assemble into a disc-shaped complex containing inner and outer rings depicted here as an orange slice. In this model, the C terminus of CAV1 is localized to the center of the complex whereas the N terminus is found on the periphery of the disc. Interactions between monomers that contribute to disc formation occur both in the outer ring and inner ring. (**B**) In the absence of an intact C terminus, CAV1 assembles into linear oligomers stabilized by interactions between adjacent monomers in the outer ring. (**C**) Along the outer ring, interactions between CAV1 monomers are predicted to occur at two binding interfaces, as opposed to primarily involving homotypic interactions between oligomerization domains of the monomers.

formation of the stalk and inner ring in this model. This can help explain why progressive truncations of the C terminus increasingly destabilize CAV1 complexes (*16*). Last, the model predicts that monomers must ultimately assemble into a closed ring to form a mature 8*S* complex. Although the exact mechanism by which this structure is generated remains to be determined, it is not difficult to imagine that it occurs via a cooperative process (*16*).

Our results also shed light on how the human CAV1 mutations F160X and P158P contribute to disease. We previously reported that both mutants are capable of generating 8*S* complexes when expressed either individually or in combination with WT CAV1 (*24*, *27*). The complexes containing F160X are destabilized compared to those formed by WT CAV1 (*24*). Our current findings suggest that this destabilization is the direct result of disruption of the central stalk together with packing defects of the protein in the center of the 8*S* complex resulting from the loss of residues 160 to 178 due to the frameshift. This model further predicts the C terminus of WT CAV1 would also fail to become incorporated into the protrusion when coexpressed with the mutant proteins. Consistent with this, we found that the C terminus of CAV1 is aberrantly exposed in caveolae in patient fibroblasts heterozygous for the F160X mutant and when coexpressed with WT CAV1 in CAV1$^{-/-}$ mouse embryonic fibroblasts (*24*). Patient cells expressing a copy of either F160X or P158P together with a copy of WT CAV1 also exhibit other abnormalities, including decreased colocalization of cavin with CAV1 in presumptive caveolae and decreased association of CAV1 with detergent resistant membranes (*24*, *27*). Our current findings implicate defects in the central region of the 8*S* complexes as giving rise to these irregularities.

Implications for how 8*S* complexes pack in caveolae and *h*-caveolae

Current models suggest that the polygonal shape of mammalian caveolae is generated by a coat complex consisting of an inner polyhedral cage formed by CAV1 surrounded by an outer filamentous layer composed of cavins (*3*, *34*). The presence of the cytoplasmic coat of cavins has made it difficult to gain further insights into the organization of 8*S* complexes within this structure. In contrast, the absence of cavins in *h*-caveolae offers the potential to directly visualize CAV1 embedded in membrane under conditions where it induces membrane curvature. Here, we were able to directly observe multiple 8*S* complexes in purified negatively stained *h*-caveolae with the help of Venus as a fiduciary marker (Fig. 5, A to C). We also detected individual 8*S*-like complexes in preparations of purified, detergent-solubilized *h*-caveolae (Fig. 5, F to H). Examples of conjoined 8*S* complexes aligned in an arc-like organization were also apparent in preparations of detergent solubilized, purified *h*-caveolae (Fig. 5, F and I). We speculate these arcs might correspond to the 200-, 400-, and 600-kDa species detected in original descriptions of caveolin oligomers (*13*). Thus, *h*-caveolae do appear to be composed of multiple copies of these discs. Assuming an average diameter of 30 nm for a typical *h*-caveola and a diameter of 14.4 nm for an 8*S* complex of CAV1-His, we estimate 12 complexes could pack on a single *h*-caveola. This is notable given that mammalian caveolae have been suggested to assume a dodecahedral architecture (*3*). Moreover, assuming that there are ~10 CAV1 monomers per 8*S* complex, each *h*-caveola would be predicted to contain ~120 copies of CAV1. This is within error of the number of caveolins that have been estimated to associate with mammalian caveola, 144 ± 39 (*35*).

More work will be required to determine exactly how CAV1 bends membranes to form *h*-caveolae and caveolae, and whether the same or different mechanisms are responsible for mammalian caveolae biogenesis and *h*-caveolae assembly. It has already been shown that a smaller region of the protein is required to form *h*-caveolae (residues 81 to 147) than to support mammalian caveolae biogenesis (residues 49 to 147) (*5*, *9*). In our experiments, deletion of residues 2 to 48 (ΔN) led to the formation of irregular complexes and linear chains, whereas a previous study showed these residues are not required for an MBP-tagged form of CAV1 to form *h*-caveolae (*9*). It is therefore possible that CAV1 may not need to assemble into stable discs to support *h*-caveolae formation. Indeed, ectopic overexpression of several different membrane proteins can generate intracellular membranes in *E. coli*, implying that several distinct molecular mechanisms may be involved (*36*). Thus, CAV1 could potentially drive membrane remodeling in this model system by more than one mechanism, depending on its organization within the membrane.

In conclusion, using electron microscopy, we have now uncovered the basic structural organization of CAV1 8*S* complexes and visualized their packing in *h*-caveolae. These findings suggest new

models for how caveolin self-assembles to form the disc-shaped oligomers that serve as building blocks for caveolae, how disease-associated mutations affect complex formation, and how these oligomers interact with one another to remodel membranes. They thus represent an important step toward resolving the long-standing question of how caveolins control the formation and function of caveolae.

MATERIALS AND METHODS

Cloning

A summary of the constructs used in this study is provided in table S2, and the primers used to generate them are described in table S3. Histidine-tagged truncations and disease-associated mutants of CAV1 were generated by polymerase chain reaction (PCR) from a pET24-CAV1-6His plasmid (a gift from K. Jebrell Glover, Lehigh University) containing a complementary DNA (cDNA) sequence of WT human CAV1 codon optimized for *E. coli* expression and cloned into a pET20 vector (Novagen no. 69739) using Nde I and Xho I restriction sites. To generate MBP-CAV1, the cDNA of human CAV1 was PCR amplified from the mammalian expression plasmid Emerald-CAV1 C-10 (Addgene no. 54025, a gift from M. Davidson) and cloned into a pNMTMA-MBP-CAV1 (canine) plasmid described in (*20*) (a gift from R. Parton, University of Queensland) using Bam HI and Eco RI restriction sites to replace the sequence of canine CAV1. To better control the expression, the human CAV1 fragment was further moved into a pET28-MBP-TEV plasmid (a gift from Z. Balklava and T. Wassmer, Addgene no. 69929) described in (*37*) using Bam HI and Eco RI restriction sites. CAV1-Venus was synthesized and subcloned into the abovementioned pET28 vector by GenScript (Piscataway, NJ). CAV1β-Venus was generated from the CAV1-Venus construct by introducing flanking Nco I and Hind III sites. After the restriction digest, the insert was ligated into the mutated pET28/Tev-mVenus-His vector, carrying a Hind III site that was added by QuikChange Lightning Site-Directed Mutagenesis (Agilent). Following the successful ligation, the Hind III site was destroyed to restore the original sequence. All constructs were confirmed by sequencing.

Detergent screening

To identify detergents that would retain oligomeric assembly of 8*S* CAV1 complexes and yield homogeneous protein samples suitable for EM studies after they were extracted from membrane, we performed FSEC screening (*21*). Initially, HeLa cells (American Type Culture Collection) transiently expressing CAV1-Venus fusion protein were solubilized with buffers composed of 200 mM NaCl, 20 mM tris-HCl (pH 8.0), 1 mM dithiothreitol (DTT), 1 mM phenylmethylsulfonyl fluoride (PMSF), and one of the following detergents: 2% *n*-decyl-β-D-maltopyranoside (C10M), 2% *n*-undecyl-β-D-maltopyranoside (C11M), 2% *n*-dodecyl-β-D-maltopyranoside (C12M), 2% CHAPS, 2% Cymal-5, 2% Cymal-6, 1% decyl neopentyl glycol, 1% glyco-diosgenin (GDN), 2% *n*-Dodecyl-*N*,*N*-Dimethylamine-*N*-Oxide (LDAO), 1% lauryl neopentyl glycol (LMNG), 2% n-nonyl-β-D-glucopyranoside (NG), 2% *n*-octyl-β-D-glucopyranoside (OG), 2% SDS, and 0.5% Triton X-100. After removing insoluble material by centrifugation at 70,000 rpm (S110AT rotor), samples were loaded to a Superose 6 Increase 10/300 GL column (GE Healthcare) equilibrated with 200 mM NaCl, 20 mM tris-HCl (pH 8.0), 1 mM DTT, and 0.005% LMNG. Elution profile of the CAV1-Venus was traced using the fluorescence signal (λ_{ex} = 500 nm; λ_{em} = 540 nm). Quality of the protein samples were judged by the sharpness and symmetry of the peaks and elution volume. After a series of screening experiments on proteins expressed in Hela cells and *E. coli*, we concluded that C12M was the most suitable detergent for extraction and purification of CAV1 8*S* complexes.

Expression of CAV1 and purification of CAV1 complexes and *h*-caveolae

Caveolin proteins were expressed in *E. coli* BL21 using the auto-induction expression system (*38*). Specifically, monoclonal bacteria were first cultured in non-inducing MDG media at 37°C and 250 rpm for 20 hours, then the cultures were enlarged in auto-inducing ZYM-5052 media at 25°C and 350 rpm for 24 hours. *E. coli* cells were resuspended with buffer [200 mM NaCl and 20 mM tris-HCl (pH 8.0)] and homogenized with pressure homogenizer (EmulsiFlex-C3 or French Press); 1 mM DTT and PMSF were added just before homogenization. Large cell debris was removed by 15 min centrifugation at 9000 rpm and 4°C. Total membranes were pelleted at 40,000 rpm (Ti-45 rotor) and 4°C for 1 hour and then were homogenized in a buffer composed of 200 mM NaCl, 20 mM tris-HCl (pH 8.0), and 1 mM DTT using a Dounce tissue grinder. Solubilization of 8*S* complexes was performed by mixing the homogenized sample at 4°C for 2 hours after addition of C12M (Anatrace) to a final concentration of 2%. After removing the insoluble material by centrifugation at 42,000 rpm (Ti-50.2 rotor) for 35 min, CAV1 was purified using nickel sepharose–based affinity purification. Elutions with CAV1 were concentrated and further purified by size exclusion chromatography using Superpose 6 Increase 10/300 GL (GE Healthcare, Illinois) equilibrated with a buffer composed of 200 mM NaCl, 20 mM tris-HCl (pH 8.0), 1 mM DTT, and 0.05% C12M.

For *h*-caveolae purification, the homogenized total membranes were directly subjected to the nickel sepharose–based purification procedure without prior detergent extraction. Where indicated, the purified *h*-caveolae were subsequently solubilized with 1% TX-100 on a rotator at 4°C for 30 min.

Electrophoresis and Western blotting

Electrophoresis (SDS-PAGE and Blue native) and Western blotting were performed as described previously (*22*, *24*, *27*). Rabbit anti-CAV1 polyclonal antibody (catalog number 610059) from BD Biosciences (San Jose, CA) was used with 1:10,000 times dilution.

Negative stain preparation and electron microscopy

Samples of purified CAV1 constructs were prepared for negative stain EM using established methods (*39*). In brief, 200-mesh copper grids covered with carbon-coated collodion film (EMS, Hatfield, PA, USA) were glow discharged for 30 s at 10 mA in a PELCO easiGlow glow discharge unit (Fresno, CA, USA). Aliquots (3.5 μl) of the CAV1 purifications (50 μg/ml) were adsorbed to the grids and incubated for 1 min at room temperature. Samples were then washed with two drops of water and stained with two successive drops of 0.7% (w/v) uranyl formate (EMS, Hatfield, PA, USA) followed by blotting until dry. Samples were visualized on a Tecnai Spirit T12 transmission electron microscope equipped with a field emission gun operating at an accelerating voltage of 120 keV (Thermo Fisher Scientific, Waltham, MA, USA) at a nominal magnification of ×26,000 (2.34 Å per pixel) or using a Thermo Fisher Scientific Tecnai T20 equipped with a field emission gun operating at an accelerating voltage of 200 keV. For the CAV1-Venus, sample low-dose data were collected using Leginon software (*23*) on a 4 k × 4 k charge-coupled device

Ultrascan camera (Gatan, Pleasanton, CA) at −1.5-μm defocus value. For all the other CAV1, sample data were collected using Leginon software on a 4 k × 4 k Rio complementary metal-oxide semiconductor camera (Gatan, Pleasanton, CA) at −1.5-μm defocus value.

Purified intact *h*-caveolae and detergent-solublized *h*-caveolae were prepared for negative-stain electron microscopy by standard methods. An aliquot was applied to glow-discharged continuous carbon grids for 1 min, blotted, and washed with three drops of water and then three drops of 2% uranyl acetate, with the final drop incubating for 1 min before blotting to dryness. The grids were imaged in an F20 electron microscopy (Thermo Fisher Scientific, formerly FEI) operating at 120 kV at magnifications ranging from ×29,000 to ×62,000, with images at 50,000× and a pixel size of 2.25 Å used for image processing.

Image processing and particle classification

Negative stain images were manually curated and images were processed using Relion 3.0.8 (*23*). For each dataset approximately 1000 particles were manually picked and subjected to 2D classification. Several of the highest resolution classes were then used as references for particle selection on all images. Particles were then extracted into 128 pixel boxes (30 nm by 30 nm) followed by 2D classification. Datasets include 16,834 particles for WT CAV1, 11,016 particles for CAV1-Venus, 15,106 for CAV1 V170X, 13,012 particles for CAV1 N173X, 37,568 particles for CAV1β-Venus, and 18,424 particles for CAV1β.

Data analysis and diameter measurements

Oval plot analysis was conducted according to the method shared by dscho on ImageJ forum (http://imagej.1557.x6.nabble.com/Circular-plot-with-ImageJ-td3687397.html). All diameter measurements were carried out using the circular en face views only. Images were downloaded from the Leginon web interface (*23*) in JPG format and opened in ImageJ (*40*). To perform diameter measurements, a spatial scale of the active image was defined by measuring a 200-nm scale bar on a single micrograph with the set scale function. Diameter measurements for each dataset were made using a line tool followed by the measure function. To obtain statistically robust results, 200 measurements were made for each dataset. Prism 8 (v8.4.2; GraphPad Software, San Diego, CA, USA) was used to plot the results and perform statistical analyses.

SUPPLEMENTARY MATERIALS

Supplementary material for this article is available at http://advances.sciencemag.org/cgi/content/full/6/49/eabc6185/DC1

View/request a protocol for this paper from *Bio-protocol*.

REFERENCES AND NOTES

1. G. E. Palade, Fine structure of blood capillaries. *J. Appl. Phys.* **24**, 1424–1436 (1953).
2. R. G. Parton, M. A. del Pozo, Caveolae as plasma membrane sensors, protectors and organizers. *Nat. Rev. Mol. Cell Biol.* **14**, 98–112 (2013).
3. M. Stoeber, P. Schellenberger, C. A. Siebert, C. Leyrat, A. Helenius, K. Grünewald, Model for the architecture of caveolae based on a flexible, net-like assembly of Cavin1 and Caveolin discs. *Proc. Natl. Acad. Sci. U.S.A.* **113**, E8069–E8078 (2016).
4. C. Lamaze, N. Tardif, M. Dewulf, S. Vassilopoulos, C. M. Blouin, The caveolae dress code: Structure and signaling. *Curr. Opin. Cell Biol.* **47**, 117–125 (2017).
5. M. Kirkham, S. J. Nixon, M. T. Howes, L. Abi-Rached, D. E. Wakeham, M. Hanzal-Bayer, C. Ferguson, M. M. Hill, M. Fernandez-Rojo, D. A. Brown, J. F. Hancock, F. M. Brodsky, R. G. Parton, Evolutionary analysis and molecular dissection of caveola biogenesis. *J. Cell Sci.* **121**, 2075–2086 (2008).
6. B. Sinha, D. Köster, R. Ruez, P. Gonnord, M. Bastiani, D. Abankwa, R. V. Stan, G. Butler-Browne, B. Vedie, L. Johannes, N. Morone, R. G. Parton, G. Raposo, P. Sens, C. Lamaze, P. Nassoy, Cells respond to mechanical stress by rapid disassembly of caveolae. *Cell* **144**, 402–413 (2011).
7. K. T. Root, J. A. Julien, K. J. Glover, Secondary structure of caveolins: A mini review. *Biochem. Soc. Trans.* **47**, 1489–1498 (2019).
8. K. T. Root, S. M. Plucinsky, K. J. Glover, Recent progress in the topology, structure, and oligomerization of caveolin: A building block of caveolae. *Curr. Top. Membr.* **75**, 305–336 (2015).
9. N. Ariotti, J. Rae, N. Leneva, C. Ferguson, D. Loo, S. Okano, M. M. Hill, P. Walser, B. M. Collins, R. G. Parton, Molecular characterization of caveolin-induced membrane curvature. *J. Biol. Chem.* **290**, 24875–24890 (2015).
10. J. Lee, K. J. Glover, The transmembrane domain of caveolin-1 exhibits a helix–break–helix structure. *Biochim. Biophys. Acta* **1818**, 1158–1164 (2012).
11. K. N. Allen, S. Entova, L. C. Ray, B. Imperiali, Monotopic membrane proteins join the fold. *Trends Biochem. Sci.* **44**, 7–20 (2019).
12. M. Sargiacomo, P. E. Scherer, Z. Tang, E. Kübler, K. S. Song, M. C. Sanders, M. P. Lisanti, Oligomeric structure of caveolin: Implications for caveolae membrane organization. *Proc. Natl. Acad. Sci. U.S.A.* **92**, 9407–9411 (1995).
13. S. Monier, R. G. Parton, F. Vogel, J. Behlke, A. Henske, T. V. Kurzchalia, VIP21-caveolin, a membrane protein constituent of the caveolar coat, oligomerizes in vivo and in vitro. *Mol. Biol. Cell* **6**, 911–927 (1995).
14. I. Fernandez, Y. Ying, J. Albanesi, R. G. W. Anderson, Mechanism of caveolin filament assembly. *Proc. Natl. Acad. Sci. U.S.A.* **99**, 11193–11198 (2002).
15. A. Hayer, M. Stoeber, C. Bissig, A. Helenius, Biogenesis of caveolae: Stepwise assembly of large caveolin and cavin complexes. *Traffic* **11**, 361–382 (2010).
16. X. Ren, A. G. Ostermeyer, L. T. Ramcharan, Y. Zeng, D. M. Lublin, D. A. Brown, Conformational defects slow Golgi exit, block oligomerization, and reduce raft affinity of caveolin-1 mutant proteins. *Mol. Biol. Cell* **15**, 4556–4567 (2004).
17. A. R. Busija, H. H. Patel, P. A. Insel, Caveolins and cavins in the trafficking, maturation, and degradation of caveolae: Implications for cell physiology. *Am. J. Physiol. Cell Physiol.* **312**, C459–C477 (2017).
18. Z. Tang, P. E. Scherer, T. Okamoto, K. Song, C. Chu, D. S. Kohtz, I. Nishimoto, H. F. Lodish, M. P. Lisanti, Molecular cloning of caveolin-3, a novel member of the caveolin gene family expressed predominantly in muscle. *J. Biol. Chem.* **271**, 2255–2261 (1996).
19. G. Whiteley, R. F. Collins, A. Kitmitto, Characterization of the molecular architecture of human caveolin-3 and interaction with the skeletal muscle ryanodine receptor. *J. Biol. Chem.* **287**, 40302–40316 (2012).
20. P. J. Walser, N. Ariotti, M. Howes, C. Ferguson, R. Webb, D. Schwudke, N. Leneva, K.-J. Cho, L. Cooper, J. Rae, M. Floetenmeyer, V. M. J. Oorschot, U. Skoglund, K. Simons, J. F. Hancock, R. G. Parton, Constitutive formation of caveolae in a bacterium. *Cell* **150**, 752–763 (2012).
21. T. Kawate, E. Gouaux, Fluorescence-detection size-exclusion chromatography for precrystallization screening of integral membrane proteins. *Structure* **14**, 673–681 (2006).
22. B. Han, A. Tiwari, A. K. Kenworthy, Tagging strategies strongly affect the fate of overexpressed caveolin-1. *Traffic* **16**, 417–438 (2015).
23. C. Suloway, J. Pulokas, D. Fellmann, A. Cheng, F. Guerra, J. Quispe, S. Stagg, C. S. Potter, B. Carragher, Automated molecular microscopy: The new Leginon system. *J. Struct. Biol.* **151**, 41–60 (2005).
24. B. Han, C. A. Copeland, Y. Kawano, E. B. Rosenzweig, E. D. Austin, L. Shahmirzadi, S. Tang, K. Raghunathan, W. K. Chung, A. K. Kenworthy, Characterization of a caveolin-1 mutation associated with both pulmonary arterial hypertension and congenital generalized lipodystrophy. *Traffic* **17**, 1297–1312 (2016).
25. A. Garg, M. Kircher, M. del Campo, R. S. Amato, A. K. Agarwal, Whole exome sequencing identifies de novo heterozygous *CAV1* mutations associated with a novel neonatal onset lipodystrophy syndrome. *Am. J. Med. Genet. A* **167**, 1796–1806 (2015).
26. I. Schrauwen, S. Szelinger, A. L. Siniard, A. Kurdoglu, J. J. Corneveaux, I. Malenica, R. Richholt, G. Van Camp, M. De Both, S. Swaminathan, M. Turk, K. Ramsey, D. W. Craig, V. Narayanan, M. J. Huentelman, A frame-shift mutation in CAV1 is associated with a severe neonatal progeroid and lipodystrophy syndrome. *PLOS ONE* **10**, e0131797 (2015).
27. C. A. Copeland, B. Han, A. Tiwari, E. D. Austin, J. E. Loyd, J. D. West, A. K. Kenworthy, A disease-associated frameshift mutation in caveolin-1 disrupts caveolae formation and function through introduction of a de novo ER retention signal. *Mol. Biol. Cell* **28**, 3095–3111 (2017).
28. E. D. Austin, L. Ma, C. LeDuc, E. B. Rosenzweig, A. Borczuk, J. A. Phillips III, T. Palomero, P. Sumazin, H. R. Kim, M. H. Talati, J. West, J. E. Loyd, W. K. Chung, Whole exome sequencing to identify a novel gene (caveolin-1) associated with human pulmonary arterial hypertension. *Circ. Cardiovasc. Genet.* **5**, 336–343 (2012).
29. S. M. Plucinsky, K. J. Glover, Secondary structure analysis of a functional construct of caveolin-1 reveals a long C-terminal helix. *Biophys. J.* **109**, 1686–1688 (2015).
30. T. Machleidt, W.-P. Li, P. Liu, R. G. W. Anderson, Multiple domains in caveolin-1 control its intracellular traffic. *J. Cell Biol.* **148**, 17–28 (2000).

31. T. Fujimoto, H. Kogo, R. Nomura, T. Une, Isoforms of caveolin-1 and caveolar structure. *J. Cell Sci.* **113**, 3509–3517 (2000).
32. R. G. Parton, M. Hanzal-Bayer, J. F. Hancock, Biogenesis of caveolae: A structural model for caveolin-induced domain formation. *J. Cell Sci.* **119**, 787–796 (2006).
33. K. S. Song, Z. Tang, S. Li, M. P. Lisanti, Mutational analysis of the properties of caveolin-1. A novel role for the C-terminal domain in mediating homo-typic caveolin-caveolin interactions. *J. Biol. Chem.* **272**, 4398–4403 (1997).
34. A. Ludwig, B. J. Nichols, S. Sandin, Architecture of the caveolar coat complex. *J. Cell Sci.* **129**, 3077–3083 (2016).
35. L. Pelkmans, M. Zerial, Kinase-regulated quantal assemblies and kiss-and-run recycling of caveolae. *Nature* **436**, 128–133 (2005).
36. N. Jamin, M. Garrigos, C. Jaxel, A. Frelet-Barrand, S. Orlowski, Ectopic neo-formed intracellular membranes in *Escherichia coli*: A response to membrane protein-induced stress involving membrane curvature and domains. *Biomolecules* **8**, 88 (2018).
37. H. Currinn, B. Guscott, Z. Balklava, A. Rothnie, T. Wassmer, APP controls the formation of PI(3,5)P_2 vesicles through its binding of the PIKfyve complex. *Cell. Mol. Life Sci.* **73**, 393–408 (2016).
38. F. W. Studier, Protein production by auto-induction in high density shaking cultures. *Protein Expr. Purif.* **41**, 207–234 (2005).
39. M. Ohi, Y. Li, Y. Cheng, T. Walz, Negative staining and image classification—Powerful tools in modern electron microscopy. *Biol. Proced. Online* **6**, 23–34 (2004).
40. C. A. Schneider, W. S. Rasband, K. W. Eliceiri, NIH Image to ImageJ: 25 years of image analysis. *Nat. Methods* **9**, 671–675 (2012).

Acknowledgments: We thank R. Parton and K. Jebrell Glover for providing plasmids, M. Elmer-Dixon and members of the Ohi Laboratory for helpful discussions, T. Wang for editorial assistance with an early draft of the manuscript, and G. Tian from Liaoning University School of Mathematics for assistance with estimating the stoichiometry of 8*S* complexes per *h*-caveola. We acknowledge M. Su, A. Bondy, L. Keopping, C. Lilienthal, B. Battey, and L. Chang for technical support. **Funding:** The University of Michigan Cryo-EM Facility (U-M Cryo-EM) has received generous support from the U-M Life Sciences Institute and the U-M Biosciences Initiative. The University of Virginia Molecular Electron Microscopy Core facility at the University of Virginia is supported in part by the School of Medicine and built with NIH grant G20-RR31199. This work was supported by NIH grants R01HL144131 (M.D.O. and A.K.K.) and S10OD020011 (LSI computation). **Author contributions:** E.K., D.P.C., H.S.M., and B.H. developed CAV1 purification procedures. B.H. and Y.P. cloned and biochemically purified all CAV1 constructs. J.C.P., J.L.H., E.B., and K.D. collected and processed the EM data. M.D.O. and A.K.K. conceived the project and provided feedback on all experiments and data processing. B.H., J.C.P., J.L.H, M.D.O, and A.K.K. wrote the initial drafts of the manuscript. All authors interpreted the data, discussed the results, and provided feedback on the final version of the manuscript. **Competing interests:** The authors declare that they have no competing interests. **Data and materials availability:** All data needed to evaluate the conclusions in the paper are present in the paper and/or the Supplementary Materials. Additional data related to this paper may be requested from the authors.

Submitted 8 May 2020
Accepted 16 October 2020
Published 2 December 2020
10.1126/sciadv.abc6185

Citation: B. Han, J. C. Porta, J. L. Hanks, Y. Peskova, E. Binshtein, K. Dryden, D. P. Claxton, H. S. Mchaourab, E. Karakas, M. D. Ohi, A. K. Kenworthy, Structure and assembly of CAV1 8*S* complexes revealed by single particle electron microscopy. *Sci. Adv.* **6**, eabc6185 (2020).